SIAM J. SCI. COMPUT.
Vol. 23, No. 4, pp. 1204–1225

THE METHOD OF REGULARIZED STOKESLETS*

RICARDO CORTEZ†

Abstract. A numerical method for computing Stokes flows in the presence of immersed boundaries and obstacles is presented. The method is based on the smoothing of the forces, leading to regularized Stokeslets. The resulting expressions provide the pressure and velocity field as functions of the forcing. The latter expression can also be inverted to find the forces that impose a given velocity boundary condition. The numerical examples presented demonstrate the wide applicability of the method and its properties. Solutions converge with second-order accuracy when forces are exerted along smooth boundaries. Examples of segmented boundaries and forcing at random points are also presented.

Key words. Stokes flow, immersed boundaries

AMS subject classifications. 76D07, 65M99, 65D32

PII. S106482750038146X

1. Introduction.

The numerical method presented here is for the computation of two- and three-dimensional Stokes flows driven by external forcing. The forces are applied on volumes or along boundaries, which may be curves, segments, or sets of disconnected points. In this way, the method applies to moving interfaces, elastic membranes interacting with a fluid, or flows through an array of fixed obstacles.

Stokes flows are of interest in many physical applications, particularly those in which the relevant length scales are extremely small or the fluid is extremely viscous. Many such applications emerge from biology, including the locomotion of bacteria and other cells, flagellated microorganisms, and flows in small capillaries. Other applications are the study of free surfaces, such as bubble motion, and flows around impurities or through a porous medium, which may be modeled as a collection of point obstacles for dilute cases.

The steady Stokes equations in two or three dimensions are

$$\mu\Delta\mathbf{u} = \nabla p - \mathbf{F}, \tag{1}$$

$$\nabla \cdot \mathbf{u} = 0, \tag{2}$$

where μ is the fluid viscosity, p is the pressure, $\mathbf{u}$ is the velocity, and $\mathbf{F}$ is force. A fundamental solution of these equations is called a *Stokeslet*, and it represents the velocity due to a concentrated external force acting on the fluid at a single point [32, 34, 1, 25]. Other, more singular solutions can also be derived from the Stokeslet by differentiation. Many important models have been created from the superposition of these fundamental solutions. Examples are analyses of flagellar motions [17, 16, 24]; the beating motion of cilia [4]; flows between plates, inside cylinders, or in periodic geometries [26, 27, 15, 33]; and slender body theories [6, 20, 23, 13]. Many of these analyses make use of images to enforce boundary conditions on the surface of spheres or planes.

*Received by the editors November 21, 2000; accepted for publication (in revised form) April 9, 2001; published electronically November 7, 2001. This work was supported in part by NSF grant DMS-9816951.

http://www.siam.org/journals/sisc/23-4/38146.html

†Department of Mathematics, Tulane University, 6823 St. Charles Ave., New Orleans, LA 70118 (cortez@math.tulane.edu).

The singularity in the Stokeslet is proportional to $1/r$ in three dimensions and $\log(r)$ in two dimensions. Consequently, when forces are concentrated on surfaces embedded in $\mathbb{R}^3$ (curves in $\mathbb{R}^2$), the expression for velocity is integrable and the flow is bounded in the vicinity of the surfaces. Most of the works cited above rely on this fact and the smoothness of the surfaces to get final expressions for the fluid velocity.

When the forces are concentrated along curves in $\mathbb{R}^3$ (points in $\mathbb{R}^2$) or when surfaces are not smooth, the situation is more difficult because the velocity formula is singular. One technique for dealing with this problem is to desingularize the expressions by introducing a small cutoff parameter in the kernels in order to regularize them. This approach has been extremely useful for the modeling of vortex motion [7, 3, 21, 14], interface motion in inviscid fluids [5, 35, 10, 8, 36], and other processes [11, 9, 12]. In all of these applications, the errors involved have been analyzed extensively and are well understood.

Our approach here is to consider the forces to be applied over a small ball, where they vary smoothly from a maximum value at the center to zero on its surface, rather than being concentrated at points (as Dirac measures). The radius of the support of the forces is a numerical parameter that can be controlled independently from any boundary discretization. Sometimes the radius of the ball is infinite, but the forces decay fast away from the center. From this starting point, expressions for the pressure and velocity due to this regularized force are derived. These expressions are bounded in any bounded set and differ only from the standard Stokeslet near the points where the forces are exerted. The resulting method is applicable to any situation in which forces drive the motion, whether they are concentrated along interfaces or points. This gives the method wide applicability. The derivation of the expressions is presented in section 2 for radially symmetric regularizations and a specific example is presented in detail. Section 3 contains several numerical examples with particular focus on the performance of the method. The case of a smooth closed boundary in $\mathbb{R}^2$ is further developed in section 4, where the velocity expressions can be written in terms of single and double layer potentials. Recent work by Beale and Lai [2] is used to achieve second-order accuracy everywhere. The final section contains concluding remarks and future directions.

2. Equations. We first consider the generic situation in which the forces are spread over a small ball centered at the points $\mathbf{x}_0$. The force is given by

$$\mathbf{F}(\mathbf{x}) = \mathbf{f}_0 \ \phi_\epsilon(\mathbf{x} - \mathbf{x}_0), \tag{3}$$

where ϕ_ϵ is a radially symmetric smooth function with the property that $\int \phi_\epsilon(\mathbf{x})d\mathbf{x} = 1$. Examples of these functions, called *blobs* or *cutoffs*, are

$$\text{in } \mathbb{R}^2: \qquad \phi_\epsilon(\mathbf{x}) = \frac{1}{\pi\epsilon^2} e^{-|\mathbf{x}|^2/\epsilon^2} \quad \text{and} \quad \phi_\epsilon(\mathbf{x}) = \frac{3\epsilon^3}{2\pi(|\mathbf{x}|^2+\epsilon^2)^{5/2}},$$

$$\text{in } \mathbb{R}^3: \qquad \phi_\epsilon(\mathbf{x}) = \frac{3}{4\pi\epsilon^3} e^{-|\mathbf{x}|^3/\epsilon^3} \quad \text{and} \quad \phi_\epsilon(\mathbf{x}) = \frac{15\epsilon^4}{8\pi(r^2+\epsilon^2)^{7/2}}.$$

A typical blob is displayed in Figure 1. The graph shows the same blob with two different values of the parameter ϵ, which controls the width, or spreading. A tighter function (smaller ϵ) must necessarily be taller for the total integral to be 1. In the limit $\epsilon \to 0$, the blob approaches a Dirac delta.

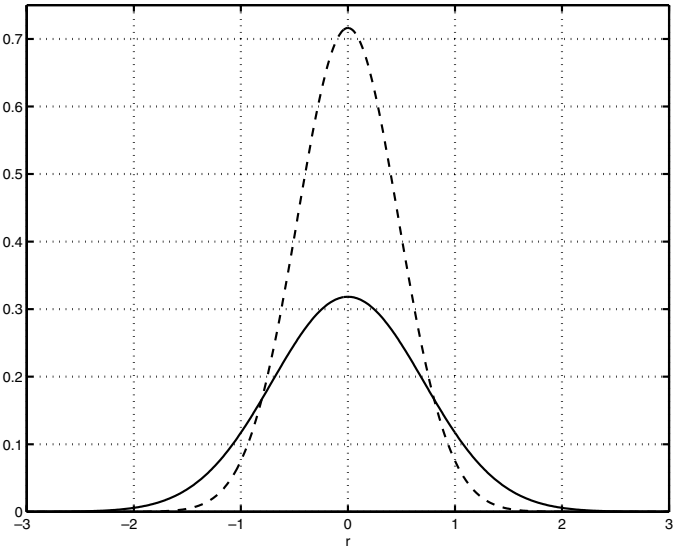

FIG. 1. *Typical blob for two different values of* ϵ.

To derive the solution of the problem in (1)–(2) in the case when the force is given by (3), we will use the following definitions. Let

$$G_\epsilon(\mathbf{x}) \text{ be the solution of } \Delta G_\epsilon = \phi_\epsilon(\mathbf{x}) \text{ in infinite space,}$$
$$B_\epsilon(\mathbf{x}) \text{ be the solution of } \Delta B_\epsilon = G_\epsilon(\mathbf{x}) \text{ in infinite space.}$$

The function $G_\epsilon(\mathbf{x})$ is a smooth approximation of the Green's function

$$\text{in } \mathbb{R}^2\text{: } G(\mathbf{x}) = \frac{1}{2\pi}\ln(|\mathbf{x}|), \qquad \text{in } \mathbb{R}^3\text{: } G(\mathbf{x}) = \frac{-1}{4\pi|\mathbf{x}|} \tag{4}$$

for $|\mathbf{x}| > \epsilon$. However, for small values of $|\mathbf{x}|$, the function G_ϵ is bounded. Similarly, $B_\epsilon(\mathbf{x})$ is smooth and approximates

$$\text{in } \mathbb{R}^2\text{: } B(\mathbf{x}) = \frac{|\mathbf{x}|^2}{8\pi}[\log(|\mathbf{x}|) - 1], \qquad \text{in } \mathbb{R}^3\text{: } B(\mathbf{x}) = \frac{-|\mathbf{x}|}{8\pi}, \tag{5}$$

which is the solution of the biharmonic equation $\Delta^2 B(\mathbf{x}) = \delta(\mathbf{x})$.

Taking the divergence of (1) and using (2) we find that the pressure satisfies

$$\Delta p = \nabla \cdot \mathbf{F},$$

which gives the particular solution

$$p = \mathbf{f}_0 \cdot \nabla G_\epsilon.$$

Now we use this expression to rewrite the equation for $\mathbf{u}$ as $\mu\Delta\mathbf{u} = (\mathbf{f}_0\cdot\nabla)\nabla G_\epsilon - \mathbf{f}_0\,\phi_\epsilon$, whose particular solution is

$$\mu\mathbf{u}(\mathbf{x}) = (\mathbf{f}_0 \cdot \nabla)\nabla B_\epsilon(\mathbf{x} - \mathbf{x}_0) - \mathbf{f}_0 G_\epsilon(\mathbf{x} - \mathbf{x}_0).$$

This might be referred to as a *regularized Stokeslet* velocity.

If there are N forces, $\mathbf{f}_k$, centered at points $\mathbf{x}_k$, the pressure and velocity are given by

$$p(\mathbf{x}) = \sum_{k=1}^{N} \mathbf{f}_k \cdot \nabla G_\epsilon(\mathbf{x} - \mathbf{x}_k), \tag{6}$$

$$\mathbf{u}(\mathbf{x}) = \mathbf{U}_o + \frac{1}{\mu} \sum_{k=1}^{N} \{(\mathbf{f}_k \cdot \nabla)\nabla B_\epsilon(\mathbf{x} - \mathbf{x}_k) - \mathbf{f}_k G_\epsilon(\mathbf{x} - \mathbf{x}_k)\}, \tag{7}$$

where we have added a constant flow $\mathbf{U}_o$ to be determined shortly. The functions G_ϵ and B_ϵ are completely determined by the blob used. They are radially symmetric just like their singular counterparts. Consequently, the velocity expression can be modified using the formulas (for $r = |\mathbf{x}|$)

$$\nabla B_\epsilon = B_\epsilon{}'(r)\frac{\mathbf{x}}{r} \quad \text{and} \quad (\mathbf{f}\cdot\nabla)\nabla B_\epsilon = \mathbf{f}\,\frac{B_\epsilon{}'(r)}{r} + (\mathbf{f}\cdot\mathbf{x})\mathbf{x}\left[\frac{rB_\epsilon{}''(r) - B_\epsilon{}'(r)}{r^3}\right],$$

which yield for $r_k = |\mathbf{x} - \mathbf{x}_k|$

$$p(\mathbf{x}) = \sum_{k=1}^{N} [\mathbf{f}_k \cdot (\mathbf{x} - \mathbf{x}_k)] \left[\frac{G_\epsilon{}'(r_k)}{r_k}\right], \tag{8}$$

$$\begin{aligned}\mathbf{u}(\mathbf{x}) = \mathbf{U}_o + \frac{1}{\mu}\sum_{k=1}^{N} \Bigg\{ &\mathbf{f}_k \left[\frac{B_\epsilon{}'(r_k)}{r_k} - G_\epsilon(r_k)\right] \\ &+ [\mathbf{f}_k \cdot (\mathbf{x} - \mathbf{x}_k)](\mathbf{x} - \mathbf{x}_k) \left[\frac{r_k B_\epsilon{}''(r_k) - B_\epsilon{}'(r_k)}{r_k^3}\right]\Bigg\}.\end{aligned} \tag{9}$$

In two dimensions, one can use (4)–(5) to check that $B'(r)/r - G(r) = -G(r)/2 - 1/8\pi$, so one can choose $\mathbf{U}_o = \sum_k \mathbf{f}_k/8\pi\mu$ in order to eliminate this remaining constant flow. In three dimensions, one can simply let $\mathbf{U}_o = \mathbf{0}$.

The method of regularized Stokeslets uses (8)–(9) to find the velocity induced by given forces. One important property of this formulation is that the flow given by (7) satisfies the incompressibility constraint $\nabla \cdot \mathbf{u} = 0$ analytically everywhere. This important property is key in the conservation of fluid volumes bounded by elastic membranes.

2.1. Deriving G_ϵ and B_ϵ. Since ϕ_ϵ is radially symmetric and $\Delta G_\epsilon = \phi_\epsilon$, we have that

$$\Delta G_\epsilon = \frac{1}{r}[rG_\epsilon{}'(r)]' = \phi_\epsilon(r)$$

and

$$G_\epsilon{}'(r) = \frac{1}{r}\int_0^r s\ \phi_\epsilon(s)ds.$$

After integrating once more, we obtain $G_\epsilon(r)$. Similarly,

$$\frac{1}{r}[rB_\epsilon{}'(r)]' = G_\epsilon(r)$$

so that $B_\epsilon(r)$ can be found in the same way.

2.1.1. A specific choice of blob in two dimensions. We present a concrete example of the regularized Stokeslet method by deriving the two-dimensional pressure and velocity formulas for the specific blob

$$\phi_\epsilon(\mathbf{x}) = \frac{3\epsilon^3}{2\pi(|\mathbf{x}|^2+\epsilon^2)^{5/2}}.$$

The corresponding regularized Green's function is

$$G_\epsilon(r) = \frac{1}{2\pi}\left[\ln\left(\sqrt{r^2+\epsilon^2}+\epsilon\right) - \frac{\epsilon}{\sqrt{r^2+\epsilon^2}}\right]$$

and

$$B_\epsilon{}'(r) = \frac{1}{8\pi}\left[2r\ln\left(\sqrt{r^2+\epsilon^2}+\epsilon\right) - r - \frac{2r\epsilon}{\sqrt{r^2+\epsilon^2}+\epsilon}\right].$$

With these functions we can write the final expressions to be used in the numerical method

$$p(\mathbf{x}) = \sum_{k=1}^{N} \frac{1}{2\pi}[\mathbf{f}_k\cdot(\mathbf{x}-\mathbf{x}_k)]\left[\frac{r_k^2+2\epsilon^2+\epsilon\sqrt{r_k^2+\epsilon^2}}{\left(\sqrt{r_k^2+\epsilon^2}+\epsilon\right)(r_k^2+\epsilon^2)^{3/2}}\right], \tag{10}$$

$$\begin{aligned}\mathbf{u}(\mathbf{x}) = &\sum_{k=1}^{N} \frac{-\mathbf{f}_k}{4\pi\mu}\left[\ln\left(\sqrt{r_k^2+\epsilon^2}+\epsilon\right) - \frac{\epsilon\left(\sqrt{r_k^2+\epsilon^2}+2\epsilon\right)}{\left(\sqrt{r_k^2+\epsilon^2}+\epsilon\right)\sqrt{r_k^2+\epsilon^2}}\right] \\ &+ \frac{1}{4\pi\mu}[\mathbf{f}_k\cdot(\mathbf{x}-\mathbf{x}_k)](\mathbf{x}-\mathbf{x}_k)\left[\frac{\sqrt{r_k^2+\epsilon^2}+2\epsilon}{\left(\sqrt{r_k^2+\epsilon^2}+\epsilon\right)^2\sqrt{r_k^2+\epsilon^2}}\right],\end{aligned} \tag{11}$$

where $r_k = |\mathbf{x}-\mathbf{x}_k|$.

One can verify that these formulas are consistent with the standard Stokeslet expressions for the case of a Dirac delta distribution of forces. Taking the limit $\epsilon \to 0$ in (10)–(11), we obtain the well-known formulas (in $\mathbb{R}^2$)

$$p(\mathbf{x}) = \sum_{k=1}^{N} \frac{[\mathbf{f}_k\cdot(\mathbf{x}-\mathbf{x}_k)]}{2\pi r_k^2}, \tag{12}$$

$$\mathbf{u}(\mathbf{x}) = \sum_{k=1}^{N} \frac{-\mathbf{f}_k}{4\pi\mu}\ln(r_k) + [\mathbf{f}_k\cdot(\mathbf{x}-\mathbf{x}_k)]\frac{(\mathbf{x}-\mathbf{x}_k)}{4\pi\mu r_k^2}. \tag{13}$$

Notice that (13) is singular at the point where the force is centered. When the sum is replaced by an integral, the velocity expression is generally not problematic when the forces are defined along smooth closed curves, since the kernel is integrable. The same is not true for the pressure which typically displays discontinuities across boundaries. A much different scenario is when the forces are defined at disconnected points, not closed curves. In this case, (12)–(13) cannot be interpreted as discretizations of integrals but simply as the superposition of singular solutions. The singularities in these formulas make the Stokeslet expression somewhat impractical for computation, since

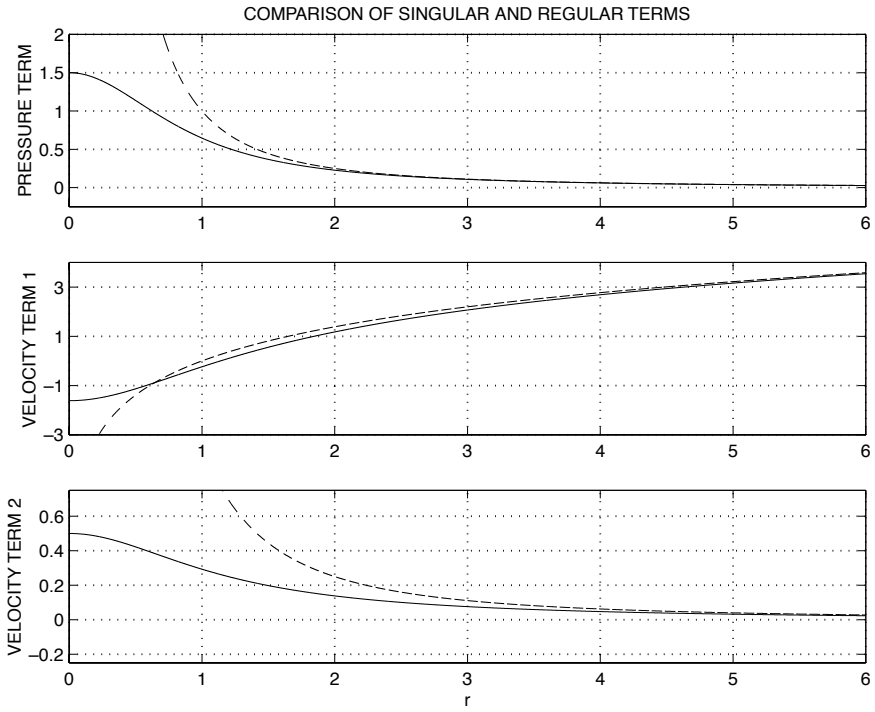

FIG. 2. *Comparison of the radial factors (in brackets) in* (10)–(11) *shown by solid lines. The regularization parameter was set to* $\epsilon = 1$. *The dashed lines are the corresponding singular terms in the Stokeslet formulas* (12)–(13).

the evaluation of the expression at a point very close to an $\mathbf{x}_k$ would lead to extremely large velocities. The regularization in (10)–(11) provides the necessary stability.

A comparison of the terms in brackets in (10)–(11) for $\epsilon = 1$ is shown in Figure 2. The smooth functions eliminate the singularity but approach asymptotically the Stokeslet expressions for $r \gg \epsilon$. In practice, the value of ϵ would be of the same order of magnitude as the particle separation in the spatial discretizations.

2.2. Finding the forces from the velocities. The numerical method derived so far can be used directly to compute the flow due to given forces. For example, elastic membranes interacting with a fluid exert forces given in terms of their configuration, which can be computed from the current position of the membrane. There are situations when the velocity of a given body is known and one is interested in finding the forces that yield that flow. Equation (9) can be used to impose velocity boundary conditions on the surface of a body. One can write, for $i = 1, \ldots, N$, the system of equations

$$\mathbf{u}(\mathbf{x}_i) = \sum_{j=1}^{N} M_{ij}(\mathbf{x}_1, \ldots, \mathbf{x}_N)\ \mathbf{f}_j$$

or, as a matrix equation,

$$\mathcal{U} = \mathcal{M}\mathcal{F}, \tag{14}$$

where, in two dimensions, $\mathcal{U}$ and $\mathcal{F}$ are $2N \times 1$ vectors and $\mathcal{M}$ is $2N \times 2N$. Generally, the matrix $\mathcal{M}$ is not invertible. This is most easily seen for the case of a closed

membrane surrounding the fluid. An arbitrary constant can be added to the normal component of the forces, causing a change in the pressure but not in the velocities because of the incompressibility of the fluid. Fortunately, any solution of the system is acceptable in the present context so that one can add the constraint that the normal component of the forces sum to zero or simply find any solution of the system via an iterative process. In this paper, we use GMRES with zero initial guess.

In steady flow problems or in situations where the geometry of the body is fixed, the matrix and any required factorization need be computed only once. In problems of moving interfaces, the matrix must be rebuilt at every time step.

3. Numerical examples.

3.1. Example 1: Flow past a cylinder. As a simple numerical experiment, consider the classical example of a circular cylinder of radius a moving at a constant speed $(1, 0)$. The exact solution is given by a combination of a Stokeslet and a dipole at the origin (see [1, p. 245]):

$$\mathbf{u}(\mathbf{x}) = \frac{-\mathbf{f}_o}{8\pi}\left(2\ln|\mathbf{x}| - a^2/|\mathbf{x}|^2\right) + \frac{(\mathbf{f}_o\cdot\mathbf{x})\mathbf{x}}{4\pi|\mathbf{x}|^2}\left(1 - a^2/|\mathbf{x}|^2\right)$$

with

$$\mathbf{f}_o = \frac{8\pi}{1-2\ln(a)}\begin{pmatrix}1\\0\end{pmatrix}.$$

Note that the velocity is unbounded as $|\mathbf{x}| \to\infty$, consistent with two-dimensional flow due to a nonzero net force (Stokes's paradox). However, the solution is valid in a region containing the cylinder.

To compute the solution with the numerical method, we discretize the circle with N particles, set the velocity at each point to $(1, 0)$, and find a vector of forces that solves the system in (14). Once the forces are known, we use (11) to find the velocity on a grid, where the exact solution is also computed for comparison. The parameters used in this example are $a = 0.25$, $N = 160$ (with $\Delta s = 2\pi a/N$), and $\epsilon = 0.25\Delta s$. Figure 3 shows the contours of the two components of velocity. Each plot shows the analytic solution (solid) and the computed solution (dashed). The velocities at the boundary points are computed with the accuracy of the iteration solver for the forces; in this case, the velocities are within 10^{-15} of their intended value.

The solutions satisfy $\|\mathbf{u}-\mathbf{u}_{exact}\|_\infty \le 2.6\times10^{-3}$ for the parameters used, although the error in the velocities is largest near the cylinder and decays nearly as $\sim |\mathbf{x}|^{-2}$ away from the boundary. In section 4, we explain how to improve on this solution. The regularization parameter ϵ is taken to be proportional to the discretization size Δs, where the proportionality constant depends on the blob ϕ_ϵ and on the particular application. In our experience, this constant is typically less than 1.

3.2. Example 2: Flow past fixed obstacles. As a second example, we consider the problem of a uniform background flow around fixed line obstacles. In this problem, the boundaries that exert forces on the fluid are not closed curves; they are disconnected line segments as shown in Figure 4. The background flow is $(1, 0)$ and two fixed line obstacles of different lengths are placed at different angles relative to the flow. The boundaries were discretized with 45 particles $\mathbf{x}_k$ (26 on the top segment and 19 on the bottom one) separated by a distance $\Delta s = 0.00447$, and the regularization parameter was set to $\epsilon = \Delta s/2$, although the solution is not very sensitive to this choice.

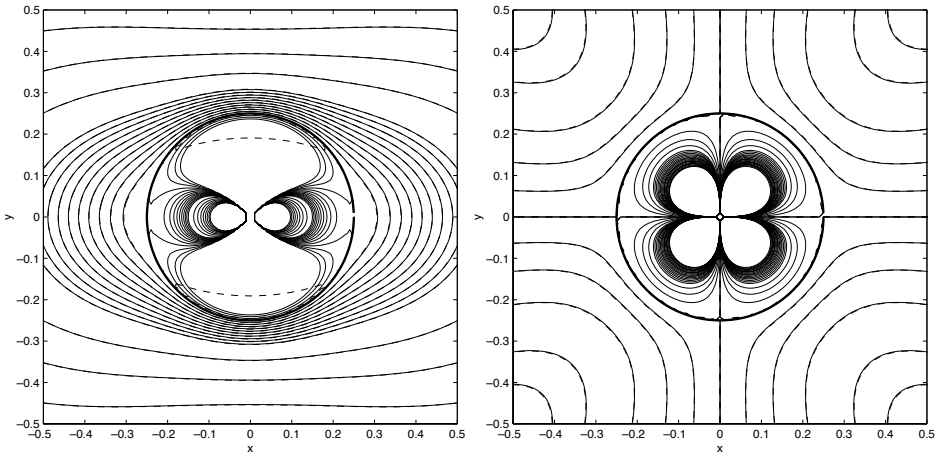

FIG. 3. *Velocity contours of the flow due to a circular cylinder of radius* $a = 0.25$ *moving with velocity* $(1, 0)$. *The left graph compares* u *in* (11) *(dashed) and the exact solution (solid). The right graph compares* v *in the same way.*

In this case, the forces on the boundaries must cancel the background flow at the $\mathbf{x}_k$'s, so the left-hand side of (14) was set to velocities corresponding to $(-1, 0)$. Once the forces are found, the flow at any point $\mathbf{x}$ is the flow induced by the forces plus the background flow. The velocity at the boundaries was no larger than 10^{-14} in magnitude. Using this steady flow computed on a regular grid, a cloud of "smoke" was advected through the obstacles for visualization purposes. This was done by solving an advection equation with the precomputed steady flow using an upwind method. The grid covered the region $[0, 1] \times [0, 0.5]$ and Neumann boundary conditions were used at the edge of the computational domain. Three snapshots are shown in Figure 4, where the fixed segments obstruct the flow and force it to go around and between them.

The same method can be used to compute the flow due to a collection of forces located at random points or the flow around a collection of point obstacles which may represent, for example, a porous medium. As an example, we consider a group of fixed particles placed randomly in a domain blocking a uniform background flow $(1, 0)$. Figure 5 shows a smaller subdomain containing 53 of the point obstacles and the flow around them. The forces at the particles are computed so that they remain stationary. The computational parameter ϵ was set to 0.03 so as to provide a resolution length scale.

3.3. Example 3: Quasi-steady flow. In this example, we consider the unsteady motion of an interface initially given in polar coordinates by $r(\theta) = \sqrt{r_o^2 - a^2/2} + a\cos(2\theta)$, where a is a perturbation amplitude. The area enclosed by this interface equals πr_o^2. The parameters used were $r_o = 0.25$ and $a = 0.05$ (see Figure 6). Since we are interested in the interface motion as it relaxes from its initial shape to a circle, we need to compute the velocity only along the interface using (11). Although the steady Stokes equations are used to compute the velocity, the time-dependent forces impose a time scale. The interface was tracked by computing the velocity as a steady flow at every time step. A similar problem was discussed in [38, 22].

Suppose $\mathbf{x}(s, t)$ defines the interface at time t in terms of the arclength parameter

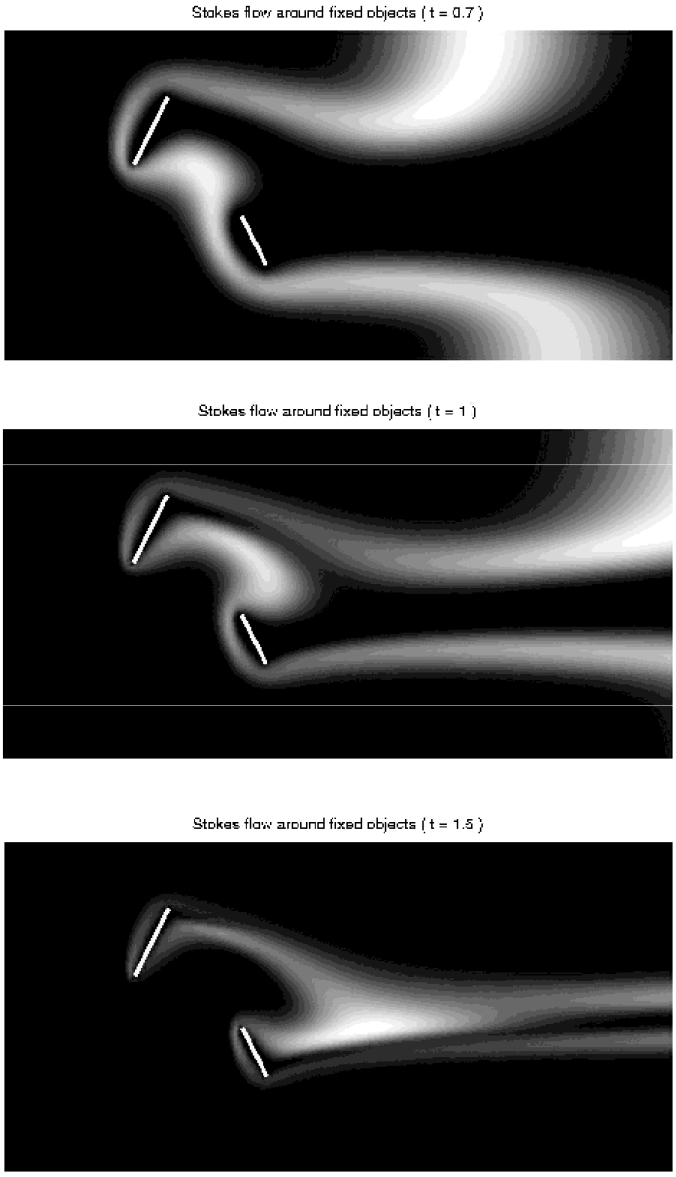

FIG. 4. *Stokes flow around two fixed line obstacles at three different times. The white cloud (initially a wide vertical stripe at the inflow) represents a quantity advected by the precomputed flow for visualization.*

s. A force

$$\mathbf{f}(s) = \frac{\partial^2 \mathbf{x}(s)}{\partial s^2} + \frac{1}{r_o}\hat{n}(s)$$

representing the curvature of the interface minus that of the final state is applied so that the shape will converge to a circle of radius r_o. This restoring force vanishes as the equilibrium state is reached. Following the suggestion in [22], one way to verify

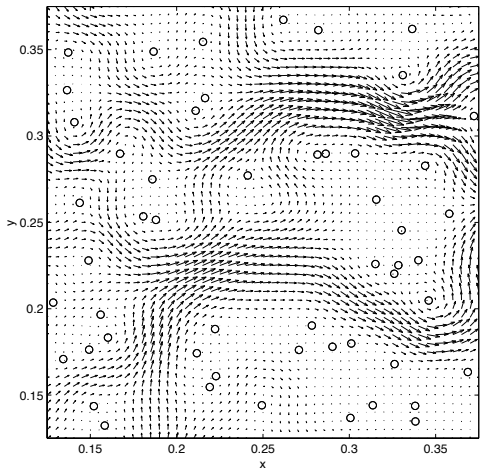

FIG. 5. *Flow around* 53 *fixed point obstacles.*

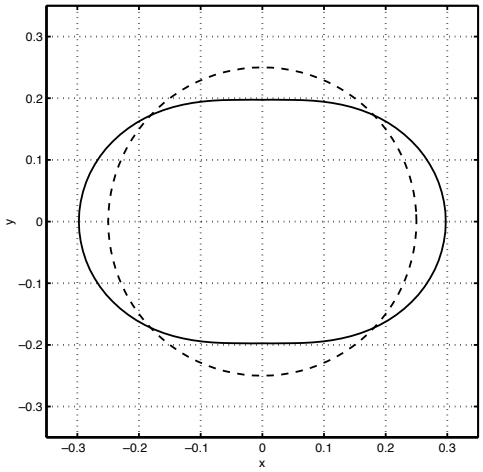

FIG. 6. *Initial shape (solid) and circle of radius* $r_o = 0.25$ *enclosing the same area.*

the shape of the final solution is to compute

$$r_{min}(t) = \min_{1 \le k \le N} \|\mathbf{x}_k(t)\| \quad \text{and} \quad r_{max}(t) = \max_{1 \le k \le N} \|\mathbf{x}_k(t)\|$$

and to check their convergence as $t \to \infty$. Figure 7 shows these results for a discretization corresponding to $N = 50$ points along the interface (equally spaced at $t = 0$). Figure 7(a) is for early times and Figure 7(b) shows the longtime behavior. The figure shows that both $r_{max}(t)$ and $r_{min}(t)$ converge to r_o. In addition, the membrane retains its circular shape indefinitely, indicating that the computation remains stable for very long times.

The interface will stop moving once the discretization errors dominate the force giving and indication of the accuracy of the method. Table 1 summarizes the results for discretizations corresponding to $N = 50$, 100, and 200. The second column of the table shows the discretization size for each run. In every case, the regularization parameter was set to $\epsilon = 1.2\Delta s$. We found this to give good results, although the

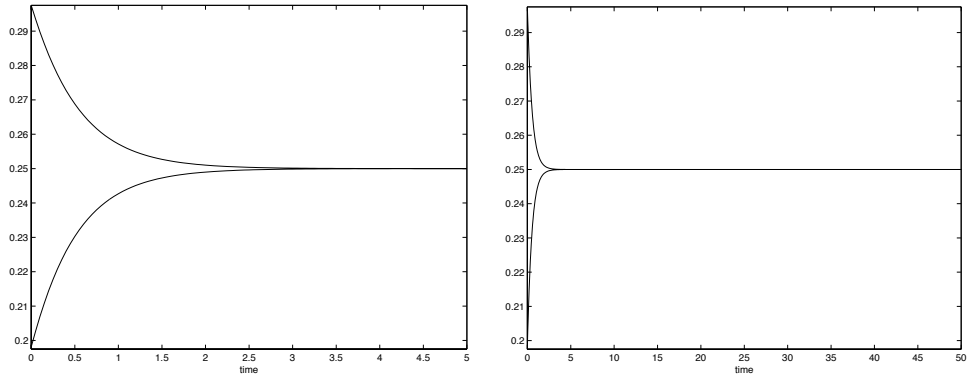

(a) (b)

FIG. 7. *Plot of $r_{max}(t)$ and $r_{min}(t)$ showing the distance from the origin to the interface as a function of time for $N = 50$ and $\epsilon = 1.2\Delta s$.* (a) *shows the plot for $0 \le t \le 5$ and* (b) *shows the plot for $0 \le t \le 50$.*

TABLE 1

Results showing r_{min}, r_{max}, area conservation A, and the magnitude of the forces for long times and various discretizations.

N	Δs	$r_{max} - r_{min}$	$\lvert A(t=50) - \pi r_o^2 \rvert$	$\lVert \mathbf{f}(t \ge 10) \rVert_\infty$
50	0.0323193	1.156836×10^{-6}	1.758022×10^{-6}	5.700275×10^{-5}
100	0.0161693	0.048211×10^{-6}	0.078004×10^{-6}	0.323780×10^{-5}
200	0.0080858	0.012735×10^{-6}	0.016602×10^{-6}	0.001307×10^{-5}

differences from other choices were not significant. The third column shows the convergence of the shape to a circle at $t = 50$; however, these numbers are essentially constant for $t \ge 10$. Note that the numbers indicate quadratic convergence in terms of Δs. The fourth column of Table 1 shows the error in the computed area inside the interface relative to the expected value πr_o^2. These numbers remained nearly constant throughout the runs. The areas were computed by discretizing a boundary integral using fourth-order finite differences. The errors in the table are within this discretization error. Finally, the last column of the table shows the maximum magnitude of the forces for $t \ge 10$ as a function of the discretization. They give an indication of the errors involved in the numerical method.

4. Modifications for closed, smooth boundaries. The case of a closed, smooth boundary is the most widely studied and one for which several numerical methods exist. This is because the situation is simplified by the absence of endpoints or by the presence of a boundary consisting of disconnected points. Techniques discussed in [34, 22, 28, 29, 30, 31, 37] are often used to compute accurate solutions of elliptic problems in general regions. In the context of fluid flow, the computation of the velocities and pressure far from the boundary or on the boundary are not typically problematic. The challenge is the computation of the solution at points very close to but off the boundary. This situation arises, for example, when the velocity is required in the entire computational domain for the advection of chemicals or solvents.

We present a modified regularization approach that leads to pointwise second-order accuracy in ϵ.

We consider a closed boundary parametrized by arclength $\mathbf{x}(s)$ for $0 \le s \le L$.

Our strategy will be to write the solution as a combination of integrals of the form

$$I_1(\mathbf{x}, f) = \int_0^L f(s)\ \mathbf{x}'(s) \times \nabla G(\mathbf{x} - \mathbf{x}(s))\ ds$$

and

$$I_2(\mathbf{x}, g) = \int_0^L g(s)\ \mathbf{x}'(s) \cdot \nabla G(\mathbf{x} - \mathbf{x}(s))\ ds$$

for some functions $f(s)$ and $g(s)$ and Green's function G. The reason is that Beale and Lai [2] have developed correction terms that can be added to the trapezoid rule applied to these integrals that guarantee second-order accuracy. To approximate these integrals, first we use the identities

$$\int_0^L \mathbf{x}'(s) \cdot \nabla G(\mathbf{x} - \mathbf{x}(s))\ ds = 0 \quad \text{for all } \mathbf{x} \text{ off the curve,}$$

$$\int_0^L \mathbf{x}'(s) \times \nabla G(\mathbf{x} - \mathbf{x}(s))\ ds = \begin{cases} 1 & \text{for } \mathbf{x} \text{ inside the boundary,} \\ 0 & \text{for } \mathbf{x} \text{ outside the boundary} \end{cases}$$

to rewrite them, for any value of s^*, as

$$I_2(\mathbf{x}, g) = \int_0^L \left[\mathbf{x}'(s) \cdot \nabla G(\mathbf{x} - \mathbf{x}(s))\right] \left[g(s) - g(s^*)\right]\ ds$$

and

$$I_1(\mathbf{x}, f) = \int_0^L \left[\mathbf{x}'(s) \times \nabla G(\mathbf{x} - \mathbf{x}(s))\right] \left[f(s) - f(s^*)\right]\ ds + \chi(\mathbf{x}) f(s^*),$$

where $\chi(\mathbf{x}) = 1$ if $\mathbf{x}$ is enclosed by the boundary and $\chi(\mathbf{x}) = 0$ otherwise. This formulation gives additional regularity to the integrands. The idea is to discretize the integrals with the trapezoid rule and to realize that when the evaluation point $\mathbf{x}$ is very near the boundary, i.e., $\|\mathbf{x} - \mathbf{x}(s)\| \leq O(\Delta s)$ for some s, the accuracy of the quadrature is compromised. However, the leading-order error terms can be identified and subtracted from the quadrature in order to achieve second-order accuracy pointwise. Therefore,

$$\begin{aligned} I_1(\mathbf{x}, f) = \sum_{k=0}^{N} \mathbf{x}'(s_k) \times \nabla G_\epsilon(\mathbf{x} - \mathbf{x}(s_k))[f_k - f(s^*)]\Delta s \\ + \chi(\mathbf{x}) f(s^*) + T_1^{(n)}(\mathbf{x}) + T_2^{(n)}(\mathbf{x}) + O(\Delta s^2), \end{aligned}$$

where the $T^{(n)}$ terms are corrections associated with the use of G_ϵ in place of G and the discretization of the integral. Similarly,

$$I_2(\mathbf{x}, g) = \sum_{k=0}^{N} \mathbf{x}'(s_k) \cdot \nabla G_\epsilon(\mathbf{x} - \mathbf{x}(s_k))[g_k - g(s^*)]\Delta s + T_1^{(t)}(\mathbf{x}) + T_2^{(t)}(\mathbf{x}) + O(\Delta s^2).$$

For each point $\mathbf{x}$ where the sum is evaluated we require s^*, which is the value of the curve parameter that identifies the boundary point closest to $\mathbf{x}$. These formulas have been derived for the specific cutoff function

$$\phi_\epsilon(r) = \frac{1}{\pi\epsilon^2} e^{-r^2/\epsilon^2}.$$

Refer to [2] for more details.

In order to write formulas for p and $\mathbf{u}$ in terms of this type of integrals, it will be convenient to use the decomposition of the forces

$$\mathbf{f}(s) = f^{(n)}\hat{n}(s) + f^{(t)}\mathbf{x}'(s),$$

where the outward normal vector is $\hat{n}(s) = (y'(s), -x'(s))$. Based on (12) we have that

$$\begin{aligned} p(\mathbf{x}) &= \int_0^L \frac{\mathbf{f}(s)\cdot(\mathbf{x}-\mathbf{x}(s))}{2\pi|\mathbf{x}-\mathbf{x}(s)|^2}\, ds = \int_0^L \mathbf{f}(s)\cdot\nabla G(\mathbf{x}-\mathbf{x}(s))\, ds \\ &= \int_0^L -f^{(n)}(s)\ \mathbf{x}'(s)\times\nabla G(\mathbf{x}-\mathbf{x}(s))\, ds + \int_0^L f^{(t)}(s)\ \mathbf{x}'(s)\cdot\nabla G(\mathbf{x}-\mathbf{x}(s))\, ds \\ &= -I_1(\mathbf{x}, f^{(n)}) + I_2(\mathbf{x}, f^{(t)}). \end{aligned} \tag{15}$$

From (13) we have

$$\begin{aligned} \mathbf{u}(\mathbf{x}) &= \int_0^L \frac{-\mathbf{f}(s)}{4\pi\mu}\ \ln|\mathbf{x}-\mathbf{x}(s)| + [\mathbf{f}(s)\cdot(\mathbf{x}-\mathbf{x}(s))]\frac{(\mathbf{x}-\mathbf{x}(s))}{4\pi\mu|\mathbf{x}-\mathbf{x}(s)|^2}\, ds \\ &= \int_0^L \left(\frac{-\mathbf{f}(s)}{2\mu}\right) G(\mathbf{x}-\mathbf{x}(s))\, ds + \int_0^L (\mathbf{x}-\mathbf{x}(s))\frac{[\mathbf{f}(s)\cdot\nabla G(\mathbf{x}-\mathbf{x}(s))]}{2\mu}\, ds. \end{aligned}$$

By defining the vector

$$\mathbf{F}(s) = \int_0^s \frac{-\mathbf{f}(\alpha)}{2\mu}\, d\alpha,$$

we can write the first integral as

$$\int_0^L \mathbf{F}(s)\ \mathbf{x}'(s)\cdot\nabla G(\mathbf{x}-\mathbf{x}(s))\, ds = I_2(\mathbf{x}, \mathbf{F}). \tag{16}$$

The second integral becomes

$$\begin{aligned} &\int_0^L (\mathbf{x}-\mathbf{x}(s))\frac{[\mathbf{f}(s)\cdot\nabla G(\mathbf{x}-\mathbf{x}(s))]}{2\mu}\, ds \\ &= \int_0^L \frac{(\mathbf{x}-\mathbf{x}(s))}{2\mu}[-f^{(n)}(s)\mathbf{x}'(s)\times\nabla G(\mathbf{x}-\mathbf{x}(s)) + f^{(t)}(s)\mathbf{x}'(s)\cdot\nabla G(\mathbf{x}-\mathbf{x}(s))]\, ds \\ &= I_1(\mathbf{x}, \mathbf{Q^a}) + I_2(\mathbf{x}, \mathbf{Q^b}), \end{aligned}$$

where

$$\mathbf{Q^a}(s) = -\frac{(\mathbf{x}-\mathbf{x}(s))f^{(n)}(s)}{2\mu}, \quad \mathbf{Q^b}(s) = \frac{(\mathbf{x}-\mathbf{x}(s))f^{(t)}(s)}{2\mu}.$$

Then,

$$\mathbf{u}(\mathbf{x}) = I_2(\mathbf{x}, \mathbf{F}) + I_1(\mathbf{x}, \mathbf{Q^a}) + I_2(\mathbf{x}, \mathbf{Q^b}). \tag{17}$$

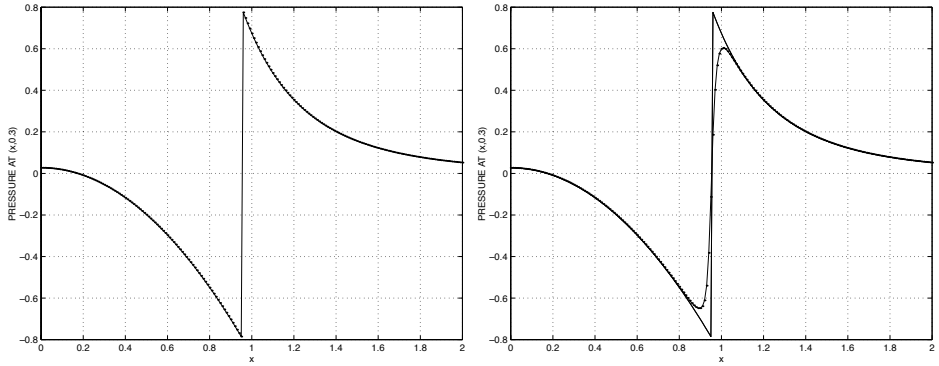

FIG. 8. (a) *Computed pressure p along the line* $(x, 3/10)$ *for* $N = 100$ *(dots) using the method of section* 4. *Also plotted is the exact (discontinuous) solution.* (b) *Pressure computed using* (10).

4.1. Example 4a: Normal forces on a circle. Consider a circular boundary of radius 1 parametrized by $\mathbf{x}(\theta) = (\cos(\theta), \sin(\theta))$ and define the forces on the boundary by

$$\mathbf{f}(\theta) = 2\sin(3\theta)\mathbf{x}(\theta)$$

so that the forces are *normal* to the boundary. The exact solution is given by

$$p(r,\theta) = \begin{cases} -r^3 \sin(3\theta), & r < 1, \\ r^{-3} \sin(3\theta), & r > 1, \end{cases}$$

$$u(r,\theta) = \begin{cases} \frac{3}{8} r^2 \sin(2\theta) + \frac{1}{16} r^4 \sin(4\theta) - \frac{1}{4} r^4 \sin(2\theta), & r < 1, \\ \frac{1}{8} r^{-2} \sin(2\theta) - \frac{3}{16} r^{-4} \sin(4\theta) + \frac{1}{4} r^{-2} \sin(4\theta), & r \geq 1, \end{cases}$$

$$v(r,\theta) = \begin{cases} \frac{3}{8} r^2 \cos(2\theta) - \frac{1}{16} r^4 \cos(4\theta) - \frac{1}{4} r^4 \cos(2\theta), & r < 1, \\ \frac{1}{8} r^{-2} \cos(2\theta) + \frac{3}{16} r^{-4} \cos(4\theta) - \frac{1}{4} r^{-2} \cos(4\theta), & r \geq 1. \end{cases}$$

We note that p is discontinuous across the boundary, but $\partial p/\partial r$, u, ∇u, v, and ∇v are continuous.

In order to show representative results, we choose to compare the solution along the line $(x, 3/10)$ for $0 < x < 2$. The boundary was discretized with N equally spaced points, and the regularization parameter was set equal to $\epsilon = 2\pi/16N$. Figures 8 and 9 show results for $N = 100$.

Figure 8(a) displays the computed pressure using the method in section 4. For larger values of N, the solutions are nearly indistinguishable from one another. The formula based on (15) is able to capture the jump in the pressure in spite of the use of regularization. This is because the jump was explicitly included in the formula for $I_1(\mathbf{x}, f)$. If instead one used (10) to compute the pressure, the effect of the regularization would be to replace the discontinuity with a rapid but smooth transition over a region of size $O(\epsilon)$, as shown in Figure 8(b). This, of course, leads to $O(1)$ errors near the interface.

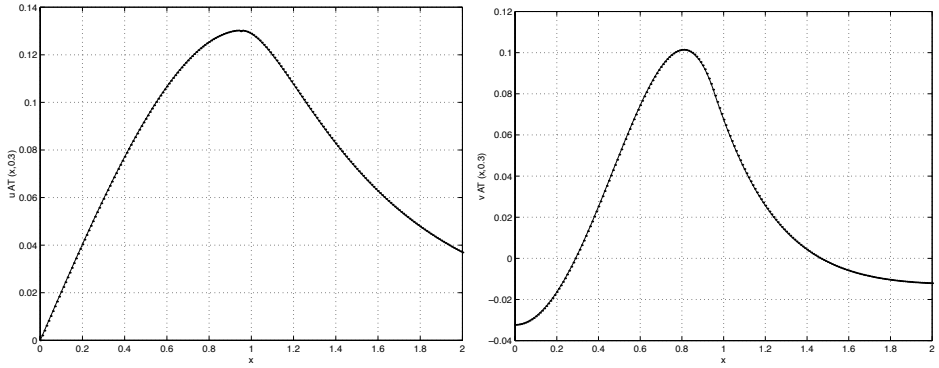

FIG. 9. *Velocity components u (left) and v (right) along the line* $(x, 3/10)$ *for* $N = 100$ *(dots). Also plotted is the exact solution (solid).*

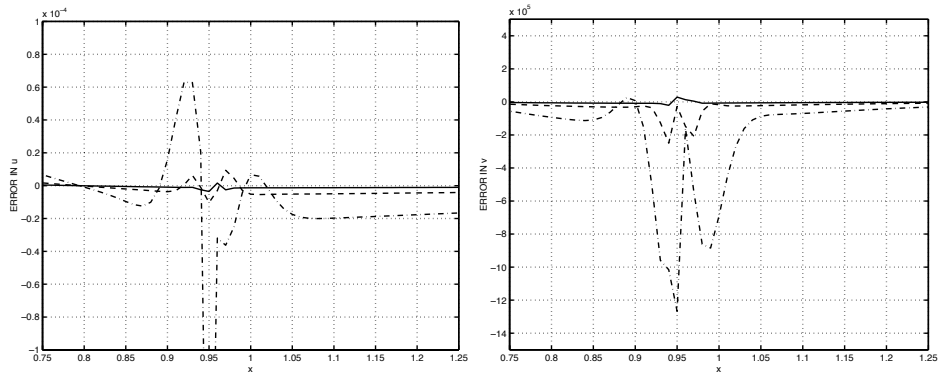

FIG. 10. *Error in the velocity components along the line* $(x, 3/10)$ *for* $N = 100$*,* 200*, and* 400*.*

The velocities are $C^1(\mathbb{R}^2)$ and this additional smoothness allows the numerical method to approximate the velocities very well everywhere, as seen in Figure 9. The largest discrepancy, however, is still near the boundary. To be more precise, we compute the error in the solution for the various discretizations. We recall that, in this example, ϵ is inversely proportional to N. Figure 10 shows the error in the velocities and Figure 11 the error in the pressure.

The largest velocity errors are $O(10^{-4})$, corresponding to the smallest value of N. More importantly, the L_2 norm of these errors, shown in Table 2, decreases by a factor of about 4 as the number of boundary points N is doubled, indicating that the pressure and velocity errors are $O(\epsilon^2)$ as $\epsilon \to 0$.

4.2. Example 4b: Tangential forces on a circle. Now consider the same circular boundary of radius 1 parametrized by $\mathbf{x}(\theta) = (\cos(\theta), \sin(\theta))$ but define the forces on the boundary by

$$\mathbf{f}(\theta) = 2\sin(3\theta)\mathbf{x}'(\theta)$$

so that the forces are now *tangential* to the boundary. The difference between this and the previous example is significant because of the character of the solution. Here, p and $\mathbf{u}$ are continuous everywhere, but their gradients are discontinuous across the

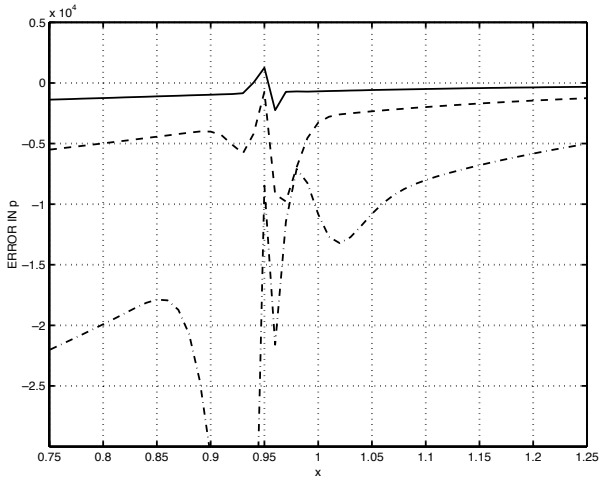

FIG. 11. *Error in the pressure along the line* $(x, 3/10)$ *for* $N = 100$, 200, *and* 400.

TABLE 2

L_2 norm of errors shown in Figures 10–11. *When the number of particles is doubled, the errors decrease by a factor of about* 4, *showing second order convergence.*

N	Error in p	Error in u	Error in v
100	25.35×10^{-4}	4.603×10^{-4}	4.656×10^{-4}
200	6.023×10^{-4}	0.781×10^{-4}	1.052×10^{-4}
400	1.468×10^{-4}	0.200×10^{-4}	0.248×10^{-4}

boundary. The exact solution is

$$p(r,\theta) = \begin{cases} -r^3 \cos(3\theta), & r < 1, \\ -r^{-3} \cos(3\theta), & r > 1, \end{cases}$$

$$u(r,\theta) = \begin{cases} \frac{1}{8} r^2 \cos(2\theta) + \frac{1}{16} r^4 \cos(4\theta) - \frac{1}{4} r^4 \cos(2\theta), & r < 1, \\ -\frac{1}{8} r^{-2} \cos(2\theta) + \frac{5}{16} r^{-4} \cos(4\theta) - \frac{1}{4} r^{-2} \cos(4\theta), & r \geq 1, \end{cases}$$

$$v(r,\theta) = \begin{cases} -\frac{1}{8} r^2 \sin(2\theta) + \frac{1}{16} r^4 \sin(4\theta) + \frac{1}{4} r^4 \sin(2\theta), & r < 1, \\ \frac{1}{8} r^{-2} \sin(2\theta) + \frac{5}{16} r^{-4} \sin(4\theta) - \frac{1}{4} r^{-2} \sin(4\theta), & r \geq 1. \end{cases}$$

Again we compare the solution along the line $(x, 3/10)$ for $0 < x < 2$, which crosses the boundary at around $x = 0.954$. The boundary was discretized with N particles (initially equally spaced), and this time the regularization parameter was set to $\epsilon = \Delta s/4$. For other values of ϵ, the results were similar. Figures 12 and 13 show the results. We note that the corners in the solution (gradient discontinuities) are captured well with the method.

The errors using $N = 100$, 200, and 400 are shown in Figure 14. The magnitude of the errors is comparable to those in the previous example, and the convergence appears to be second order as well.

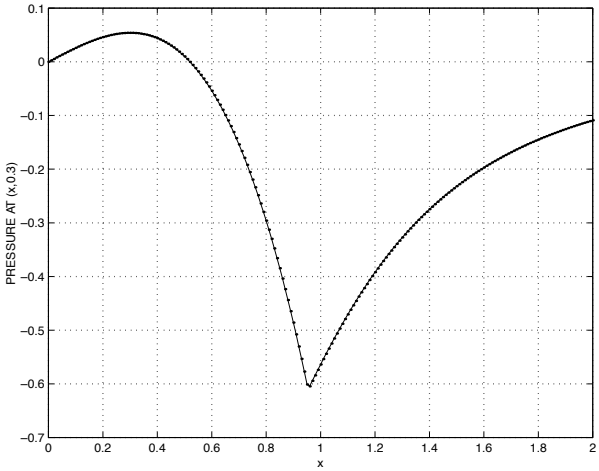

FIG. 12. *Computed pressure p along the line $(x, 3/10)$ for $N = 100$ (dots). Also plotted is the exact solution (solid).*

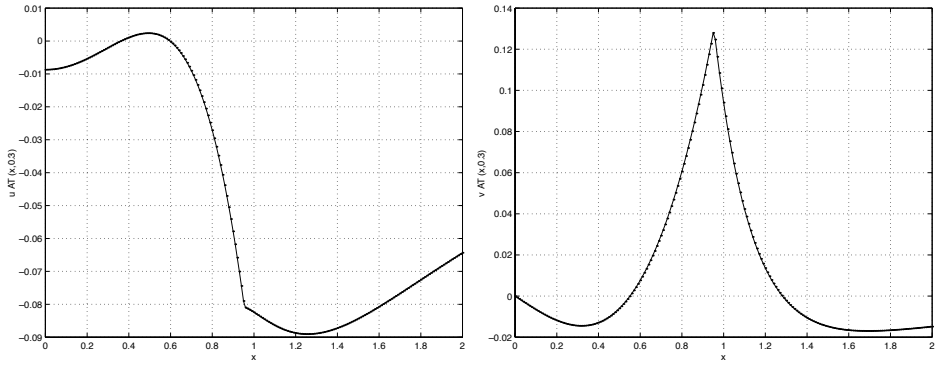

FIG. 13. *Computed velocity components u (left) and v (right) along the line $(x, 3/10)$ for $N = 100$ (dots). Also plotted is the exact solution (solid).*

We make one more comment about the choice of the regularization parameter ϵ in the present context. While it is usually taken as $\epsilon = O(\Delta s)$, the errors in computing integrals of the form

$$\int_0^L \hat{n}(s) \cdot \nabla G(\mathbf{x} - \mathbf{x}(s))[f(s) - f(s^*)]ds$$

or

$$\int_0^L \mathbf{x}'(s) \cdot \nabla G(\mathbf{x} - \mathbf{x}(s))[g(s) - g(s^*)]ds$$

are slightly different when the evaluation point $\mathbf{x}$ is near, but off, the curve. This is because

$$\nabla G(\mathbf{x} - \mathbf{x}(s^*)) = \frac{\mathbf{x} - \mathbf{x}(s^*)}{2\pi|\mathbf{x} - \mathbf{x}(s^*)|^2} = \frac{\hat{n}(s^*)}{2\pi|\mathbf{x} - \mathbf{x}(s^*)|},$$

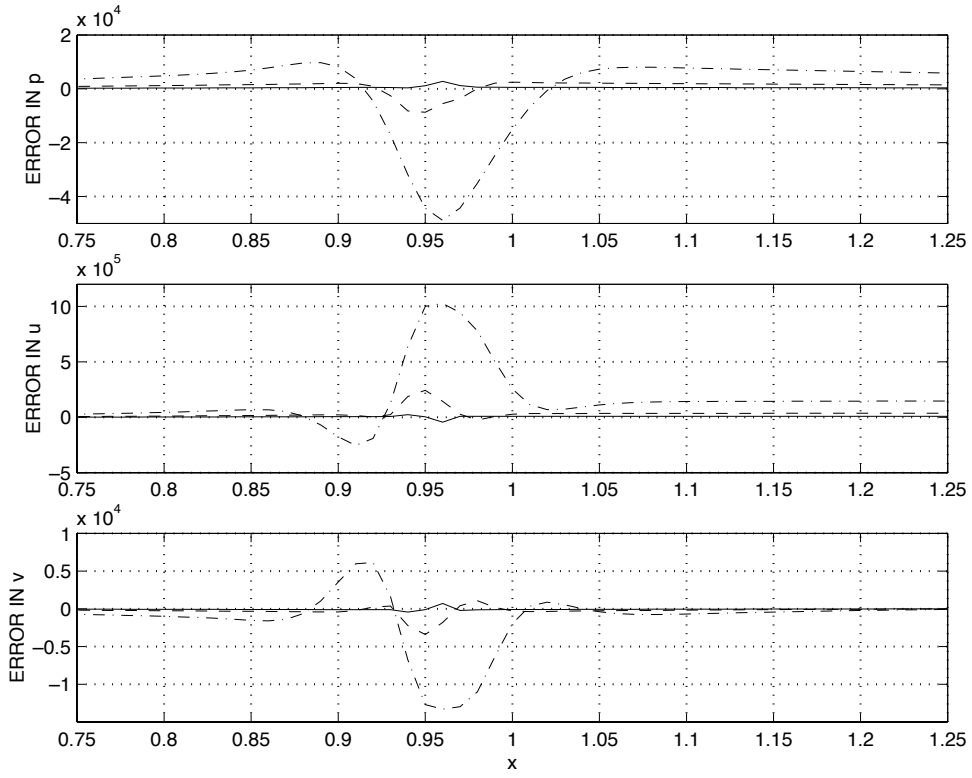

FIG. 14. *Error in the pressure and velocity components for Example* 4b. *The errors are measured along the line* $(x, 3/10)$ *for* $N = 100$, 200, *and* 400.

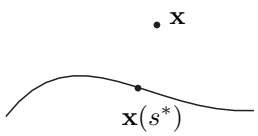

FIG. 15. *Schematic diagram.*

which implies that for $s \approx s^*$ (see Figure 15)

$$\hat{n}(s) \cdot \nabla G(\mathbf{x} - \mathbf{x}(s)) \sim \frac{O(1)}{|\mathbf{x} - \mathbf{x}(s^*)|},$$

while

$$\mathbf{x}'(s) \cdot \nabla G(\mathbf{x} - \mathbf{x}(s)) \sim \frac{O(s - s^*)}{2\pi|\mathbf{x} - \mathbf{x}(s^*)|},$$

so that the first integrand above is "more nearly singular" than the second. This somewhat affects the optimal size of ϵ relative to Δs.

4.3. Numerical example 5: Computing stresses. We consider a final example of flow in a channel obstructed by a semicircular protrusion (see Figure 16). This problem has been studied in [19] as a model for the adhesion of a cell to the wall of a channel and the stresses exerted on these cells by fluid flowing within the channel. Additional numerical studies of this problem are found in [39] and a variant of it

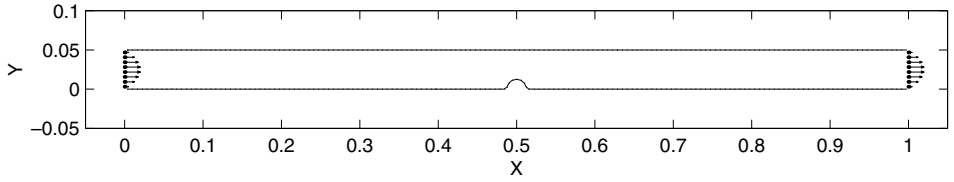

FIG. 16. *Geometry of the problem and velocity boundary conditions.*

in [18]. The objective is to determine the stresses along the channel walls, including the obstruction. It is assumed that the flow is driven by a constant pressure gradient and has reached a steady state. In our case, the corners where the semicircle meets the channel wall have not been smoothed with fillets. The velocity inflow and outflow conditions were assumed to be the parabolic Poiseuille flow, while the fluid velocity at the channel walls was set to zero.

Using the nondimensionalization in [19], the parameters used were $\Delta p = 1$, $\mu = H^2/8L^2$, $L = 1$, and $H = 0.05$, where L and H are the length and height of the channel. The radius of the obstruction was set to $R = H/4$. A particle separation of $\Delta s = 0.0025$ was used along the straight horizontal boundaries and approximately the same on the semicircle and the inflow/outflow ends. The regularization parameter was set to $\epsilon = \Delta s/4$. To simulate the flow induced by the constant pressure gradient, a constant force $(\Delta p, 0)$ was imposed on a grid covering the interior of the channel. The velocity due to this force was computed on the channel walls using (11). As a second step, the forces along the channel walls are computed with (14) so that the desired boundary conditions, including the parabolic inflow/outflow, are obtained. The resulting boundary forces were then used to compute the normal and shear stresses on the bottom part of the channel. This was done by decomposing the forces into the normal and tangential components along the channel walls. The results are shown in Figure 17.

The shear stress has been normalized by the shear stress on a channel without the obstruction. This allows one to see that away from the obstruction, the shear stress approaches that of the free channel. Also apparent from the graph is that the maximum shear stress is nearly three times that of the flat wall. On the other hand, the normal stress is nearly equal to the pressure which decreases linearly from $p(0) = 1$ to $p(L) = 0$. The obstruction merely slightly perturbs this profile. These results are nearly identical to those shown in Figure 5 of [19] with the exception of the values at the points where the semicircle meets the wall. In [19], this corner was smoothed with small fillets to minimize the oscillation observed here, where no smoothing was used.

5. Concluding remarks. We have introduced a numerical technique for the computation of force-driven Stokes flows. At the core of the method is the regularized Stokeslet, which gives the solution due to the regular force field in (3). The standard Stokeslet is recovered in the limit as the regularization parameter vanishes. Several examples were presented that demonstrate the use of the method when the forces are applied at random points, flexible or solid boundaries. The results show that the motion of the immersed boundaries is captured very well. The volume conservation is excellent due to the exact satisfaction of the incompressibility condition in the formula (7). The solution off the boundaries is also computed accurately with a slightly modified formulation in terms of single and double layer potentials. These

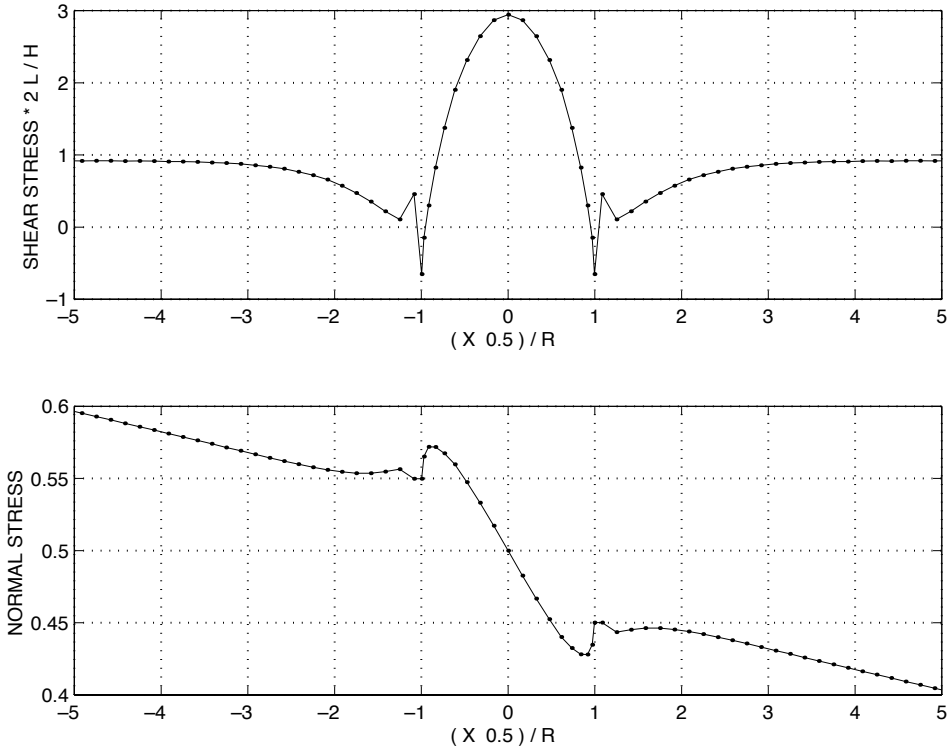

FIG. 17. *Shear and normal stresses along the bottom wall of the channel.*

results can be combined when the velocity in the entire domain is required in order to track other quantities advected by the flow.

Velocity boundary conditions can be satisfied to great precision by inverting the velocity equation and solving for the forces on the boundaries. Thus far, this has been done by the iterative procedure GMRES, although other techniques and associated preconditioners are being considered for future implementations. The resulting forces can also be used to determine stresses along walls, producing profiles without excess noise.

There are other singular solutions of Stokes equations that are also important for many applications. Elements such as dipoles, rotlets, and stresslets can be derived by applying certain differential operators to the Stokeslet. One can derive the regularized versions of these elements from the regularized Stokeslet. Regularized dipoles are already used in other fluid flow applications [5, 10, 35].

Another future direction of research is the extension of this work to three dimensions. In principle, this is already done here, since the derivation of the formulas is identical. For the simulation of bubbles or waving surfaces, these can be combined with existing triangulation or other discretization techniques. We expect to report on this case in a future article.

REFERENCES

[1] G. K. BATCHELOR, *An Introduction to Fluid Dynamics*, Cambridge University Press, Cambridge, UK, 1967.

[2] J. T. BEALE AND M.-C. LAI, *A method for computing nearly singular integrals*, SIAM J. Numer.

Anal., 38 (2001), pp. 1902–1925.
[3] J. T. Beale and A. Majda, *High order accurate vortex methods with explicit velocity kernels*, J. Comput. Phys., 58 (1985), pp. 188–208.
[4] J. R. Blake, *A model for the microstructure in ciliated organisms*, J. Fluid Mech., 55 (1972), pp. 1–23.
[5] T. F. Buttke, *Velicity methods: Lagrangian numerical methods which preserve the Hamiltonian structure of incompressible fluid flow*, in Vortex Flows and Related Numerical Methods, J. T. Beale, G.-H. Cottet, and S. Huberson, eds., NATO Adv. Sci. Inst. Ser. C Math. Phys. Sci. 395, Kluwer Academic Publishers, Dordrecht, The Netherlands, 1993, pp. 39–57.
[6] S. Childress, *Mechanics of Swimming and Flying*, Cambridge University Press, Cambridge, UK, 1981.
[7] A. J. Chorin, *Numerical study of slightly viscous flow*, J. Fluid Mech., 57 (1973), pp. 785–796.
[8] R. Cortez, *An impulse-based approximation of fluid motion due to boundary forces*, J. Comput. Phys., 123 (1996), pp. 341–353.
[9] R. Cortez, *Convergence of high-order deterministic particle methods for the convection-diffusion equation*, Comm. Pure Appl. Math., 50 (1997), pp. 1235–1260.
[10] R. Cortez and D. A. Varela, *The dynamics of an elastic membrane using the impulse method*, J. Comput. Phys., 138 (1997), pp. 224–247.
[11] P. Degond and S. Mas-Gallic, *The weighted particle method for convection-diffusion equations part* 1: *The case of an isotropic viscosity*, Math. Comp., 53 (1989), pp. 485–507.
[12] D. Fishelov, *A new vortex scheme for viscous flows*, J. Comput. Phys., 86 (1990), pp. 211–224.
[13] S. Gueron and N. Liron, *Ciliary motion modeling, and dynamic multicilia interactions*, Biophys. J., 63 (1992), pp. 1045–1058.
[14] O. H. Hald, *Convergence of vortex methods for Euler's equations* II, SIAM J. Numer. Anal., 16 (1979), pp. 726–755.
[15] H. Hasimoto, *On the periodic fundamental solutions of the Stokes equations and their applications to viscous flow past a cubic array of spheres*, J. Fluid Mech., 5 (1959), pp. 317–328.
[16] J. J. L. Higdon, *The generation of feeding currents by flagellar motions*, J. Fluid Mech., 94 (1979), pp. 305–330.
[17] J. J. L. Higdon, *A hydrodynamic analysis of flagellar propulsion*, J. Fluid Mech., 90 (1979), pp. 685–711.
[18] J. J. L. Higdon, *Stokes flow in arbitrary two-dimensional domains: Shear flow over ridges and cavities*, J. Fluid Mech., 159 (1985), pp. 195–226.
[19] D. P. Gaver III and S. M. Kute, *A theoretical model study of the influence of fluid stresses on a cell adhering to a microchannel wall*, Biophys. J., 75 (1998), pp. 721–733.
[20] J. B. Keller and S. I. Rubinow, *Slender-body theory for slow viscous flow*, J. Fluid Mech., 75 (1976), pp. 705–714.
[21] R. Krasny, *Desingularization of periodic vortex sheet roll-up*, J. Comput. Phys., 65 (1986), pp. 292–313.
[22] R. J. LeVeque and Z. Li, *Immersed interface methods for Stokes flow with elastic boundaries or surface tension*, SIAM J. Sci. Comput., 18 (1997), pp. 709–735.
[23] J. Lighthill, *Flagellar hydrodynamics*, SIAM Rev., 18 (1976), pp. 161–230.
[24] J. Lighthill, *Helical distributions of Stokeslets*, J. Engrg. Math., 30 (1996), pp. 35–78.
[25] J. Lighthill, *Mathematical Biofluiddynamics*, SIAM, Philadelphia, 1975.
[26] N. Liron and S. Mochon, *Stokes flow for a Stokeslet between two parallel flat plates*, J. Engrg. Math., 10 (1976), pp. 287–303.
[27] N. Liron and R. Shahar, *Stokes flow due to a Stokeslet in a pipe*, J. Fluid Mech., 86 (1978), pp. 727–744.
[28] A. Mayo, *The fast solution of Poisson's and the biharmonic equations on irregular regions*, SIAM J. Numer. Anal., 21 (1984), pp. 285–299.
[29] A. Mayo, *The rapid evaluation of volume integrals of potential theory on general regions*, J. Comput. Phys., 100 (1992), pp. 236–245.
[30] A. Mayo and C. S. Peskin, *An Implicit Numerical Method for Fluid Dynamics Problems with Immersed Elastic Boundaries*, Contemp. Math. 141, AMS, Providence, RI, 1993, pp. 261–277.
[31] A. McKenney, L. Greengard, and A. Mayo, *A fast Poisson solver for complex geometries*, J. Comput. Phys., 118 (1995), pp. 348–355.
[32] C. Pozrikidis, *Boundary Integral and Singularity Methods for Linearized Viscous Flow*, Cambridge University Press, Cambridge, UK, 1992.
[33] C. Pozrikidis, *On the transient motion of ordered suspensions of liquid drops*, J. Fluid Mech., 246 (1993), pp. 301–320.
[34] C. Pozrikidis, *Introduction to Theoretical and Computational Fluid Dynamics*, Oxford Uni-

versity Press, Oxford, UK, 1997.
[35] M. C. Recchioni and G. Russo, *Hamilton-based numerical methods for a fluid-membrane interaction in two and three dimensions*, SIAM J. Sci. Comput., 19 (1998), pp. 861–892.
[36] M. Shelley and T. Ueda, *The Stokesian hydrodynamics of flexing, stretching filaments*, Phys. D, 146 (2000), pp. 221–245.
[37] J. Strain, *Fast potential theory* II: *Layer potentials and discrete sums*, J. Comput. Phys., 99 (1992), pp. 251–270.
[38] C. Tu and C. S. Peskin, *Stability and instability in the computation of flows with moving immersed boundaries: A comparison of three methods*, SIAM J. Sci. Statist. Comput., 13 (1992), pp. 1361–1376.
[39] H. A. R. Williams, L. J. Fauci, and D. P. Gaver III, *Evaluation of interfacial fluid dynamical stresses using the immersed boundary method*, SIAM J. Sci. Comput., submitted.